Coupling of Kinetic and Mass Transfer Processes in Direct Methanol Fuel Cells

Srikanth Arisetty,[a,*] Ulrike Krewer,[b,c] Suresh G. Advani,[a] and Ajay K. Prasad[a,z]

[a]*Center for Fuel Cell Research, Department of Mechanical Engineering, University of Delaware, Newark, Delaware 19716, USA*
[b]*Max Planck Institute for Dynamics of Complex Technical Systems, D-39106 Magdeburg, Germany*
[c]*Portable Energy Systems, Chair for Process Systems Engineering, Otto-von-Guericke University, D-39106 Magdeburg, Germany*

A model coupling momentum transport with reaction kinetics within the five-layer membrane electrode assembly has been developed for direct methanol fuel cells (DMFCs). The model accounts for the essential intermediate reaction steps on both anode and cathode catalyst layers, as well as the two-phase phenomena in the anode and cathode gas diffusion layers. The kinetics of the methanol reaction on the cathode catalyst layer that separately account for both chemical and electrochemical pathways are investigated. The model predictions agree with the DMFC experimental data. Simulation results indicate that the transport of methanol is essential in determining both the anode and cathode kinetics. Anode kinetics are not significantly improved for anode concentrations above 2 M. It is also revealed that the transport of methanol to the anode catalyst layer is significantly enhanced by the convection of CO_2 bubbles toward the flow field. The influence of methanol crossover on the cathode potential is quantified by changing the anode feed from methanol to hydrogen. The cathode potential is seen to deteriorate at higher methanol feed concentrations mainly due to the depletion of oxygen by the crossed over methanol on the cathode catalyst. This model should prove useful in optimizing the methanol feed concentration in DMFCs.

The direct conversion of chemical energy to electrical energy in direct methanol fuel cells (DMFC) is strongly influenced by the coupling of chemical kinetics with transport processes. Such systems are particularly attractive for compact, portable power applications because the high energy density of liquid fuels such as methanol permits operation over extended durations. However, the commercialization of these devices is hindered by technical issues such as the sluggish kinetics of electrochemical methanol oxidation and high rates of methanol crossover. Low catalyst activity at both the anode and cathode increases their respective overpotentials, and the propensity for methanol crossover additionally depolarizes the cathode overpotential. These shortcomings adversely impact DMFC efficiency and power density.

Recent research activity in DMFCs has focused on the development of new catalysts and membranes. Alternate Pt-free catalysts are being introduced to replace costly Pt–Ru alloy catalysts.[1] Furthermore, alternate membranes are being tested to reduce methanol crossover. The effect of membrane properties on methanol crossover has been studied extensively both experimentally and theoretically.[2,3] It is necessary to develop a fundamental understanding of the underlying physiochemical phenomena to design catalysts and membranes with the optimal composition. In addition to the development of materials, system issues such as water management, gas management, flow field design, and its optimization are also important to improve the reliability, efficiency, and durability of DMFCs.[4,5]

Several investigations have been carried out to gain a better understanding of the physiochemical processes in DMFCs. Many ex situ experiments and kinetic models have been reported that illustrate the reaction mechanisms.[6] They all show that both anode and cathode overpotentials degrade the performance of DMFCs. Similarly, visualization studies in DMFCs have indicated that transport processes such as gas management of CO_2 and the diffusion of methanol across the membrane affect the reaction kinetics.[2,7,8] However, it is very difficult to experimentally quantify and decouple the transport effect from reaction kinetics. An accurate mathematical model is highly desirable to understand these complex mechanisms and serve as a powerful tool to gain insight into each process and evaluate the various parameters that limit performance.

Early efforts on the formulation of mathematical models relied on a semiempirical approach[9-11] in which mass transport is lumped together with reaction kinetics. In semiempirical models crossover is also approximated as a constant voltage loss. Kulikovsky's model[12,13] included the two-phase flow in the anode channels. He reported that CO_2 bubbles improve or reduce performance depending on the availability of oxygen in the cathode compartment. He also proposed an expression to determine the optimal concentration of methanol for maximum electrical performance. However, his analytical model does not separately account for mass transport, the crossover effect, and the kinetic parameters. Yang and Zhao[14] developed a two-phase mass transport model for DMFCs accounting for the convection of gas in the flow fields, gas diffusion layer (GDL), and the porous catalyst layer. Their model investigates the influence of structural and operating parameters on cell performance. Similar models were also developed by Wang and Wang[15] with a focus on methanol transport in the GDL. Basic membrane electrode assembly (MEA) models were developed by Krewer et al.[16] to investigate the effect of the microporous layer on anode performance. Yin's model[17] mainly examines water and methanol crossover across the membrane. None of the models mentioned above emphasize reaction kinetics and their relation to transport processes in DMFCs.

Understanding the reaction pathways of methanol oxidation and oxygen reduction on catalyst layers is quite challenging. Kauranen et al.[18] studied the kinetics of methanol oxidation on carbon-supported Pt and Pt–Ru bonded with poly(tetrafluoroethylene) (PTFE). They developed a model and obtained rough estimates of rate constants and activation energies at low methanol concentrations. Their model supports the hypothesis that water is adsorbed as hydroxyl on the Ru catalyst, and it is the only potential-dependent reaction step. Methanol oxidation on the Pt catalyst is enhanced by the presence of Ru, as Pt is responsible for methanol adsorption and desorption, and Ru for OH adsorption.[18,19] Other researchers[6] developed rate expressions for the electrochemical oxidation of methanol at various concentrations. They found that four different kinetic expressions approximately model the experimentally observed behavior of methanol oxidation. Apart from concentration and flow rates, the effects of thermal activation on the oxidation pathways of methanol on bulk Pt–Ru alloy electrodes have also been studied.[20]

Similar to anode reaction steps, the kinetic mechanism of oxygen reduction on the cathode catalyst is also well-studied in the literature. However, the presence of methanol complicates the reaction pathways. Antoine et al.[21] and Jerkiewicz et al.[22] studied the oxygen

* Electrochemical Society Student Member.
z E-mail: prasad@udel.edu

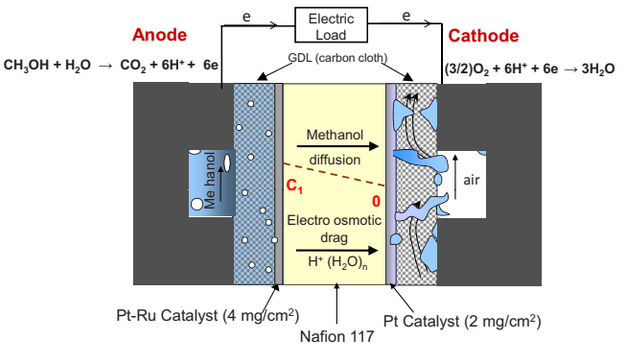

Figure 1. (Color online) DMFC schematic showing different chemical processes.

reduction reaction (ORR) mechanism on Nafion-bonded Pt particles. Oxygen reduction undergoes a series of electrochemical and chemical steps. It is debated in the literature whether the reaction intermediates are O_2H_{ads} or OH_{ads}. The intermediates vary depending on the potential of the catalyst layer.[23] For the cathode potentials measured in our DMFC, the intermediate step involves O_2H.[23] The electrochemical impedance studies performed by Antoine et al.[21] demonstrate the presence of two electrochemical steps in the ORR mechanism. Finally, it was validated that the ORR follows the (electrode chemical electrode step) ECE-Damjanovic mechanism on Pt nanoparticles inside Nafion.[21]

However, the kinetic models developed in the literature do not consider the mass transport effect on reaction kinetics. More details on the cathode and anode kinetic models are presented in the Anode kinetic model and Cathode kinetic model sections. In this study, a comprehensive model is developed to describe the two-phase flow in the anode and cathode GDL and to evaluate detailed anode and cathode kinetics. Our goal is to incorporate the physics and chemistry of the process in a comprehensive model for the MEA in DMFCs.

Mathematical Model

The schematic diagram of a DMFC with the pertinent processes is shown in Fig. 1. The nonlinear mathematical model of the DMFC is formulated to incorporate the physics and chemistry of the following phenomena:

1. Diffusive transport of methanol across the GDL.
2. Through-plane convection of methanol across the GDL to the catalyst layer.
3. Convective transport of CO_2 and water across GDL.
4. Oxidation of methanol on Pt–Ru catalyst through three-step mechanism.
5. Crossover of methanol across the membrane by diffusion.
6. Reduction of oxygen on cathode catalyst layer through two steps.
7. Oxidation of methanol on the cathode catalyst layer through chemical and electrochemical pathways.
8. Convective transport of water across the cathode GDL.

The model assumes that all material parameters are time-independent, the GDL is isotropic, gases obey ideal laws, and methanol solution is an incompressible Newtonian liquid. In addition, we assume that

1. The fuel cell is operated isothermally.
2. The bulk concentration of methanol in the flow field is averaged to the supplied methanol concentration.
3. Oxygen and CO_2 do not diffuse in the polymer electrolyte membrane.
4. The mass transport resistance in the catalyst layer and in the flow field is negligible.
5. All of the methanol that crosses over to the cathode catalyst layer reacts completely.
6. There is no flow through the membrane due to the pressure difference.
7. The electro-osmotic drag of methanol in the membrane is negligible compared to the diffusive transport of methanol.
8. The ohmic drop in the current collectors and electrical interconnects is negligible.
9. CO_2 produced does not dissolve in the liquid.
10. The concentration of water and methanol in the anode compartment is constant.
11. The relative humidity of the inlet and outlet air is always 100%.
12. Liquid water in the cathode compartment does not vaporize.

Anode model development.— Anode kinetic model.— Methanol oxidation on the anode catalyst layer can follow numerous pathways with various reaction intermediates. Kinetic models representing the methanol oxidation reaction on the catalyst layer have evolved over time. Experimentally observed steady-state behavior of the anode reaction can be exemplified by four different kinetic models.[6] One of the uncertainties in the model developed by Vidakovic et al.[6] is whether the reaction between the adsorbed methanol and OH_{ads} is potential dependent or potential independent. However, Krewer et al.[24] used electrochemical impedance spectroscopy as a dynamic tool to discriminate between the different kinetic formulations given by Vidakovic et al. Besides kinetic constants, storage parameters and potential dependence also show a strong influence on impedance spectra. The final quantitative description of the steady-state behavior developed by Krewer et al. is used to describe our anode kinetic mechanisms

$$\mathrm{Pt} + \mathrm{CH_3OH} \overset{r_{A1},k_{A1}}{\rightarrow} \mathrm{PtCO} + 4\mathrm{H^+} + 4\mathrm{e^-} \quad [1]$$

$$\mathrm{Ru} + \mathrm{H_2O} \underset{r_{-A2},k_{-A2}}{\overset{r_{A2},k_{A2}}{\rightleftharpoons}} \mathrm{RuOH} + \mathrm{H^+} + \mathrm{e^-} \quad [2]$$

$$\mathrm{PtCO} + \mathrm{RuOH} \overset{r_{A3},k_{A3}}{\rightarrow} \mathrm{CO_2} + \mathrm{H^+} + \mathrm{e^-} \quad [3]$$

The overall rate of methanol oxidation has been modeled with the reaction mechanisms and intermediates discussed earlier. In the first step, methanol adsorbs on the Pt catalyst and subsequently decomposes to CO_{ads}, protons, and electrons (Eq. 1). This decomposition step is followed by multiple additional steps. However, it is assumed that potential-independent methanol physisorption is the rate-determining step. Therefore, the rate expression (Eq. 4) describing Reaction 1 does not have a direct dependence on potential.[24] At the same time, water undergoes dissociative adsorption on the Ru catalyst forming OH_{ads}, protons, and electrons (Eq. 2). This is the only reversible intermediate step during the oxidation of methanol on the anode catalyst layer. In the final step, the surface reaction of CO_{ads} and OH_{ads} leads to the evolution of CO_2. A rate expression for each reaction is presented next

$$r_{A1} = k_{A1}(1 - \theta_{CO})C^{ac}_{meoh} \exp[-\beta_{CO} g_{CO}(\theta_{CO} - 0.5)] \quad [4]$$

$$r_{A2} = k_{A2}(1 - \theta_{OH})\exp\left(\frac{aF\eta_A}{RT}\right)\exp[-\beta_{OH} g_{OH}(\theta_{OH} - 0.5)] \quad [5]$$

$$r_{-A2} = k_{-A2}\theta_{OH} \exp\left(-\frac{(1-a)F\eta_A}{RT}\right)\exp[(1-\beta_{OH}) g_{OH}(\theta_{OH} - 0.5)] \quad [6]$$

$$r_{A3} = k_{A3}\ \exp[(1 - \beta_{CO})g_{CO}(\theta_{CO} - 0.5)]\theta_{CO}\theta_{OH} \quad [7]$$

Only Eq. 5 and 6 depend on the anode potential.[24] The concentration of water is assumed to be constant as it is in excess in the anode compartment. To evaluate the anode overpotential and coverage of adsorbed intermediates, balance equations for the adsorbed intermediates are as follows

$$c_{pt}^{ac}\frac{d\theta_{CO}^{ac}}{dt} = r_{A1} - r_{A3} \quad [8]$$

$$c_{ru}^{ac}\frac{d\theta_{OH}^{ac}}{dt} = r_{A2} - r_{-A2} - r_{A3} \quad [9]$$

$$c_A\frac{d\eta_A}{dt} = i_{cell} - 4Fr_{A1} - Fr_{A2} + Fr_{-A2} - Fr_{A3} \quad [10]$$

The solution of Eq. 8-10 cannot be obtained without knowing the methanol concentration on the anode catalyst layer. The value of the methanol concentration on the anode catalyst layer is coupled with the two-phase mass transfer expressions in the anode GDL. Therefore, to evaluate the surface coverages and the anode overpotential, Eq. 4-10 need to be solved along with the two-phase mass transport equations in porous media.

Two-phase modeling in the anode GDL.— Momentum balance.— Equations governing the two-phase regime are mass, momentum, and species conservation. The porous GDL is taken as the domain through which species entering and exiting the boundary are conserved. Methanol undergoes the reaction on the anode catalyst layer, and hence, mass and momentum conservation are applied across the boundary of GDL. The flow of methanol, water, and CO_2 across the porous GDL is governed by Darcy's law.

Applying Darcy's law to the liquid phase gives

$$u_l = -K\frac{k_{rl}}{\mu_l}\nabla P_l \quad [11]$$

Similarly, for the gaseous phase we have

$$u_g = -K\frac{k_{rg}}{\mu_g}\nabla P_g \quad [12]$$

where K is the absolute permeability, and k_{rl} and k_{rg} are the relative permeabilities of the liquid and the gaseous phase, respectively. Most GDLs made from carbon cloth are wet-proofed with PTFE.[14] The liquid and gas pressures are related to the capillary pressure by a relation which involves surface tension, porosity, and liquid saturation

$$P_c = P_g - P_l = \sigma\ \cos\ \theta_c\left(\frac{\epsilon}{K}\right)^{0.5}J(s) \quad [13]$$

In Eq. 13, s is the liquid saturation in the porous medium and $J(s)$ represents the Leverette function.[25] Hydrophobic and hydrophilic media are represented by different Leverette functions, and θ_c is the contact angle of the fluid with the solid surface

$$J(s) = \begin{cases} 1.417(1-s) - 2.12(1-s)^2 + 1.263(1-s)^3 & \text{if } \theta_c \le 90^\circ \quad \text{(hydrophilic)} \\ 1.417s - 2.12s^2 + 1.263s^3 & \text{if } \theta_c \ge 90^\circ \quad \text{(hydrophobic)} \end{cases} \quad [14]$$

The relative permeabilities in Eq. 11 and 12 are defined as a function of saturation. Liquid- and gas-phase permeabilities are given by $(1 - s)^3$ and s^3, respectively. In a hydrophobic medium, the wetting phase is the gas phase, and hence, the Leverette function is expressed in terms of the liquid-phase saturation. Similarly, for a hydrophilic medium, the gas-phase saturation is used. Hydrophobicity can be introduced by treating the GDL with PTFE. In Eq. 14, the degree of hydrophobicity in porous media is expressed in terms of the contact angle.

Mass balance.—Methanol supplied to the anode flow field arrives at the anode catalyst layer by convection and diffusion. The transported methanol reacts on the anode catalyst layer producing gaseous carbon dioxide. The emerging gas bubbles flow back into the anode flow field. Some gas bubbles end up blocking the pores in the anode GDL, which reduces the space available for methanol to diffuse. At the same time, the flux of gas bubbles emerging from the anode catalyst layer to the flow field also promotes liquid convection and mixing. Therefore, methanol transport within the GDL must account for both the diffusive and convective components.

Empirical correlations for the effective mass diffusivity through porous media have been reported in the literature.[26-28] However, Nam and Kaviany[29] suggested a correlation for the effective diffusivity in the GDL as a function of liquid saturation. We have used this correlation to formulate the mass diffusivity of reactants in the anode and cathode GDLs as a function of saturation and porosity. Our model assumes that the PTFE-treated carbon cloth can be approximated as an isotropic porous medium

$$D_{meoh}^{GDL} = D_{meoh,water}\epsilon\left(\frac{\epsilon - 0.11}{1 - 0.11}\right)^{0.785}s^2 \quad [15]$$

where $D_{meoh,water}$ is the diffusion coefficient of methanol in water and ϵ is the porosity of the anode GDL. Convective transport of methanol across the GDL is modeled using the Darcy velocity as the convective velocity. Hence, one can use Eq. 11 to express the average molar convective flux of methanol toward the catalyst layer as follows

$$R_{meoh}(\text{convective}) = -K\frac{k_{rl}}{\mu_l}\nabla P_l C_{meoh}^{ac} \quad [16]$$

Equation 16 is the simplified form of the convective transport of methanol. The through-plane convective transport is due to the inertial movement of gas bubbles through the GDL. The reaction of methanol on the anode catalyst layer causes large volume expansion due to the generation of CO_2 bubbles, which induces convection in the GDL. Other types of convective motion such as under-rib convection and mixing caused by bubble movement in porous media are possible. We neglect under-rib convection due to the high viscosity of water, and mixing effects from bubble motion are ignored for simplicity. Along with the reaction on the anode catalyst layer, methanol also diffuses toward the cathode catalyst layer through the membrane. All the methanol that crosses over to the cathode reacts completely on the cathode catalyst layer. Therefore, the concentration of methanol on the cathode catalyst layer is taken as zero. The mass flux of methanol that crosses over is given by

$$r_{crossover,meoh} = D_{meoh}^{mem}\frac{C_{meoh}^{ac}}{d_{mem}} \quad [17]$$

Using Eq. 4 and 15-17, the rate at which the methanol concentration changes on the anode catalyst layer is given as follows

$$\frac{V^{ac}}{A}\frac{dC_{meoh}^{ac}}{dt} = -K\frac{k_{rl}}{\mu_l}\nabla P_l C_{meoh}^{ac} + \frac{D_{meoh,water}}{d_{aGDL}}\epsilon\left(\frac{\epsilon - 0.11}{1 - 0.11}\right)^{0.785} \times s^2(C_o - C_{meoh}^{ac}) - r_{A1} - r_{crossover,meoh} \quad [18]$$

Now let us consider the gas-phase motion of CO_2 in the porous anode GDL. It is assumed that the gas phase consists of only CO_2

without any methanol vapor or water vapor. The average velocity of CO_2 bubbles through the GDL can be calculated using Darcy's law, which is given by Eq. 12. Based on Eq. 12 and 7, the mass rate of CO_2 generation on the cathode catalyst is given by

$$\frac{V^{ac}}{A}\frac{dC_{CO_2}}{dt} = -K\frac{k_{rg}\rho_g}{M_{CO_2}\mu_g}\nabla P_g - r_{A3} \quad [19]$$

To obtain the liquid saturation s in Eq. 15 and 18, an expression for the mass balance of water across the GDL is required. Along with methanol, water also crosses from the anode to the cathode side, reducing the water concentration in the anode compartment.[30] The amount of water that diffuses across the membrane is insignificant when compared to the water that crosses the membrane by electro-osmosis. Therefore, in our model, the electro-osmotic drag of water through the membrane is considered and diffusion is neglected. The total convective transport of liquid water and methanol toward the catalyst layer can be derived from Eq. 11 and 16. Therefore, the mass rate of water accumulation in the anode catalyst layer is given by

$$\frac{1}{A}\frac{dm_{H_2O}}{dt} = -K\frac{k_{rl}\rho_l}{\mu_l}\nabla P_l - M_{meoh}\left(-K\frac{k_{rl}}{\mu_l}\nabla P_l C^{ac}_{meoh}\right) - M_{H_2O}\left(r_{A2} - r_{-A2} + \alpha\frac{i_{cell}}{6F}\right) \quad [20]$$

where α is the electro-osmotic drag coefficient of water across the membrane.[2] Equation 11-20 characterize the two-phase transport phenomena in the anode of DMFCs. Solving Eq. 8-10, 13, and 18-20 allows one to find the surface coverages θ_{CO} and θ_{OH}, the anode overpotential, the anode catalyst layer methanol concentration, water saturation in the GDL, and the pressure drops of liquid and gas. At steady state, the time derivatives in the above set of equations are set to zero, which gives

$$r_{A1} - r_{A3} = 0 \quad [21]$$

$$r_{A2} - r_{-A2} - r_{A3} = 0 \quad [22]$$

$$-i_{cell} + 4Fr_{A1} + Fr_{A2} - Fr_{-A2} + Fr_{A3} = 0 \quad [23]$$

$$-K\frac{k_{rl}}{\mu_l}\nabla P_l C^{ac}_{meoh} + \frac{D_{meoh,water}}{d_{aGDL}}\epsilon\left(\frac{\epsilon - 0.11}{1 - 0.11}\right)^{0.785} s^2(C_o - C^{ac}_{meoh}) - r_{A1} - r_{crossover,meoh} = 0 \quad [24]$$

$$-K\frac{k_{rl}\rho_g}{M_{CO_2}\mu_g}\nabla P_g - r_{A3} = 0 \quad [25]$$

$$-K\frac{k_{rl}\rho_l}{\mu_l}\nabla P_l - M_{meoh}\left(-K\frac{k_{rl}}{\mu_l}\nabla P_l C^{ac}_{meoh}\right) - M_{H_2O}\left(r_{A2} - r_{-A2} + \alpha\frac{i_{cell}}{6F}\right) = 0 \quad [26]$$

$$P_g - P_l - \sigma\cos\theta_c\left(\frac{\epsilon}{K}\right)^{0.5} J(s) = 0 \quad [27]$$

Solving Eq. 21-27 iteratively under selected operating conditions and material variables, the steady-state values of θ_{CO}, θ_{OH}, η_A, saturation s, C^{ac}_{meoh}, ΔP_l, and ΔP_g can be calculated.

Cathode model development.— Cathode kinetic model.— It is necessary to identify the important reaction pathways within the DMFC cathode to quantify the cathode overpotential. Reduction of oxygen in H_2/O_2 proton exchange membrane (PEM) fuel cells is similar to the ORR in DMFCs. In the DMFC cathode, along with oxygen reduction, methanol that crosses over from the anode side also oxidizes, producing CO_2 and H_2O. The mixed potential effect of the electrochemical oxidation of methanol on the Pt catalyst has been studied and included in many fuel cell models. However, electrochemical experiments performed by Vielstich et al.[31] and Paganin et al.[32] suggest that methanol oxidizes both chemically and electrochemically. Additional results discussing these pathways are reported elsewhere.[33] Our cathode kinetic model is formulated considering the methanol oxidation reaction (MOR) and ORR mechanisms in the set of equations given below

$$Pt + O_2 + H^+ + e^- \overset{r_{C1},k_{C1}}{\rightarrow} PtO_2H \quad [28]$$

$$PtO_2H + 3H^+ + 3e^- \underset{r_{-C2},k_{-C2}}{\overset{r_{C2},k_{C2}}{\rightleftharpoons}} Pt + 2H_2O \quad [29]$$

$$Pt + CH_3OH \overset{r_{C3},k_{C3}}{\rightarrow} PtCO + 4H^+ + 4e^- \quad [30]$$

$$PtCO + H_2O \overset{r_{C4},k_{C4}}{\rightarrow} Pt + CO_2 + 2H^+ + 2e^- \quad [31]$$

$$PtCO + \frac{1}{2}O_2 \overset{r_{C5},k_{C5}}{\rightarrow} CO_2 + Pt \quad [32]$$

In Eq. 28, oxygen adsorbs on the Pt catalyst, forming the PtO_2H intermediate. Several intermediate configurations such as O_{ads} or OH_{ads} exist; however, it is commonly agreed that the reaction in Eq. 28 is the rate-determining step. In the next step, PtO_2H desorbs, producing water and free Pt surfaces. The cathode kinetics represented by Eq. 28 and 29 are similar to the cathode kinetics in H_2/O_2 PEM fuel cells. Subsequently, methanol adsorbs on the Pt catalyst forming the PtCO intermediate. The formation of the PtCO intermediate reduces the free Pt surface available for oxygen reduction. The mechanism of methanol oxidation on platinum has been discussed in the Anode kinetic model section. Finally, the adsorbed PtCO intermediate undergoes either electrochemical oxidation or chemical oxidation, as shown in Eq. 31 or 32, respectively. Based on the experimental observations reported in the literature, each reaction is defined to follow either Langmuir or Tempkin adsorption kinetics for which the rate expressions are formulated as follows

$$r_{C1} = k_{C1}(1 - \theta^{cc}_{CO} - \theta^{cc}_{O_2H})C^{cc}_{O_2}\exp\left[-\frac{(1-a)}{RT}F\eta_c\right] \quad [33]$$

$$r_{C2} = k_{C2}\theta^{cc}_{O_2H}\exp\left[-\frac{(1-a)}{RT}F\eta_c\right] \quad [34]$$

$$r_{-C2} = k_{-C2}(1 - \theta^{cc}_{CO} - \theta^{cc}_{O_2H})\exp\left(-\frac{a}{RT}F\eta_c\right) \quad [35]$$

$$r_{C3} = D^{mem}_{meoh}\frac{C^{ac}_{meoh}}{d_{mem}} \quad [36]$$

$$r_{C4} = k_{C4}\theta^{cc}_{CO}\exp\left(\frac{aF}{RT}\eta_c\right)\exp[(1-\beta)(\theta^{cc}_{CO} - 0.5)g_{CO}] \quad [37]$$

$$r_{C5} = k_5\theta_{CO}(C^{cc}_{O_2})^{1/2} \quad [38]$$

Equations 33 and 34 were developed based on the Langmuir isotherm of oxygen adsorption.[34] From our crossover measurements, all the methanol arriving at the cathode oxidizes completely on the cathode catalyst layer. The first step in MOR is the adsorption of methanol on the Pt catalyst. Therefore, the rate of the reaction in Eq. 30 is determined by the molar flux of methanol crossover. Finally, the rate expressions for the electrochemical and chemical oxidation of methanol were modeled based on Temkin/Frumkin kinetics. To evaluate the cathode overpotential and surface coverages, balance equations are formulated as follows

$$c^{cc}_{pt}\frac{d\theta^{cc}_{O_2H}}{dt} = r_{C1} - r_{C2} + r_{-C2} \quad [39]$$

$$c_{pt}^{cc}\frac{d\theta_{CO}^{cc}}{dt} = r_{C3} - r_{C4} - r_{C5} \quad [40]$$

$$c_C\frac{d\eta_C}{dt} = -i_{cell} + Fr_{C1} + 3r_{C2} - 3Fr_{-C2} - 4Fr_{C3} - 2Fr_{C4} \quad [41]$$

To determine the surface coverages and overpotential on the cathode catalyst layer, the concentration of oxygen on the cathode catalyst layer needs to be determined in Eq. 39-41. The kinetic model is strongly coupled to the two-phase model by the oxygen concentration on the cathode catalyst layer. Therefore, a two-phase model describing water flow in the GDL is developed.

Two-phase modeling in the cathode GDL of DMFC.— On the cathode, air or oxygen that is supplied to the cathode flow channel transfers to the catalyst layer, where oxygen is reduced forming water. As formulated in Eq. 20, water is also transported from the anode compartment to the cathode catalyst layer by electro-osmosis. The produced water, along with crossover water, is transported to the cathode flow channel through the cathode GDL. Water in the flow channel is removed either by evaporation or by the drag force of the flowing air. However, some amount of liquid water blocks the GDL pores, reducing the area available for oxygen to diffuse. Therefore, understanding water transport across the GDL is necessary to evaluate the oxidant mass flux to the catalyst layer.

Inside the cathode GDL, water is driven to the cathode flow field by capillary forces. The capillary action is a result of the capillary pressure gradient given by Eq. 13. The liquid pressure gradient is formed from higher to lower saturation regions. Because water is produced in the cathode catalyst layer, the liquid saturation in the catalyst layer is higher than in the GDL. Therefore, liquid is driven from the catalyst layer toward the flow field. Because the gas phase is open to cathode oxidant flow, the gas phase pressure will be zero relative to the liquid phase pressure. Based on the momentum conservation (Eq. 11) and the capillary (Eq. 13), the molar flux of water driven by capillary action is given as

$$R_{H_2O} = -K\frac{k_{rl}\rho_l}{M_{H_2O}\mu_l}\nabla P_c \quad [42]$$

where the capillary pressure is given by the following equation

$$\nabla P_c = -\nabla P_l = \sigma\cos\theta_c\left(\frac{\epsilon}{K}\right)^{1/2}\nabla J(s) \quad [43]$$

Capillary action can be increased by making the GDL more hydrophobic. In our model, we assumed that the oxidant is supplied at 100% relative humidity, and hence, water evaporation into the gas phase is neglected. Based on our assumptions and on Eq. 35, 37, and 43, the rate of change of water concentration on the cathode catalyst layer is given by

$$\frac{V^{cc}}{A}\frac{dC_{H_2O}^{cc}}{dt} = \frac{\alpha i}{F} + 2r_{C2} - r_{C4} - R_{H_2O} \quad [44]$$

Air is transported toward the cathode catalyst layer by both diffusion and convection. The effective mass diffusivity of the reactant through the anode GDL toward the catalyst layer is defined in Eq. 15. Similarly, the empirical correlation for the effective mass diffusivity in the cathode GDL is defined in terms of gas saturation. The empirical correlation given in the literature[29] is a function of saturation and porosity. In the case of the serpentine channel, convective bypass or under-rib convection forces the flow of reactants through the GDL under the land region, as described in detail by Feser et al.,[35] whereas the portion of the GDL under the channel itself is subjected to only diffusive transport. Due to the high Peclet number in the GDL under the land, the in-plane convective transport of oxygen dominates over diffusive transport. The through-plane convection of oxidant is also neglected. With these assumptions, the diffusive transport of oxygen toward the cathode catalyst layer can be expressed as follows

$$R_{O_2}(\text{diffusive}) = \left(\frac{b}{b+w}\right)\frac{D_{O_2,air}}{d_{cGDL}}\epsilon\left(\frac{\epsilon - 0.11}{1 - 0.11}\right)^{0.785}(1-s)^2 \times (C_{O_2}^{o} - C_{O_2}^{cc}) \quad [45]$$

In a serpentine channel, the reactant stream is forced through a single, long channel which causes a large overall pressure drop. The high gas velocity along the channel can result in the buildup of a significant pressure drop between two adjacent channels. This pressure difference can lead to a "short-circuit" of gases from one channel to the next through the porous GDL under the land that separates the two adjacent channels. Such convective transport is termed "convective bypass" or "under-rib convection," and the resulting short-circuiting of gases improves gas transport and benefits cell performance. To formulate the average convective transport of air under the land, the air velocity in the GDL is required. Feser et al.[35] provided an expression for the mean air velocity along the length of the channel (x direction) in the GDL under the land for the case of a serpentine flow field. The mean velocity of air in the channel is

$$u(x) = -\frac{k_c}{2\mu L}\frac{\Delta P_{cell}}{N_c}\left(\frac{m\cosh[m(x/L - 1/2)]}{\sinh(m/2)}\right) \quad [46]$$

and the mean velocity of air in the GDL is

$$v(x) = -\frac{k_{eff}}{2\mu b}\frac{\Delta P_{cell}}{N_c}\left(\frac{m\sinh[m(x/L - 1/2)]}{\sinh(m/2)} + 1\right) \quad [47]$$

where

$$m^2 = \frac{4L^2}{A}\frac{d_{cGDL}}{b}\frac{K_i}{K_c} \quad [48]$$

Using the expressions for the velocities of air in the channel (Eq. 46) and in the GDL (Eq. 47), along with the knowledge of oxidant flow rate (Q), the mass conservation equation of the oxidant across the cathode channel configuration is formulated below

$$N_c\int_0^L v(x)d_{cGDL}dx + N_c\frac{\int_0^L u(x)whdx}{L} = Q \quad [49]$$

Equation 49 is used to evaluate the pressure drop across the cathode of the fuel cell in terms of channel dimensions, GDL dimensions, and oxidant flow rate. Subsequently, the average air velocity in the GDL is obtained using Eq. 46, 47, and 49.

$$V_{GDL} = \frac{\int_0^L u(x)}{L} = \sqrt{\frac{K_i}{bd_{cGDL}}}\frac{1}{2LN_c}\frac{Q}{\left(\frac{1}{2}\sqrt{\frac{K_i d_{cGDL}}{b}} + \frac{\sqrt{K_c wh}}{L}\right)} \quad [50]$$

Using Eq. 50, the convective transport of air toward the catalyst layer is given by

$$R_{O_2}(\text{convective}) = \left(\frac{b}{b+w}\right)V_{GDL}(1-s)^2C_{O_2}^{cc} \quad [51]$$

Using Eq. 33, 38, 44, and 50, the rate of change of oxygen concentration in the cathode catalyst layer can be determined as follows

$$\frac{V^{cc}}{A}\frac{dC_{O_2}^{cc}}{dt} = R_{O_2}(\text{diffusive}) + R_{O_2}(\text{convective}) - r_{C1} - \frac{r_{C5}}{2} \quad [52]$$

Equations 43-51 describe the two-phase transport phenomena in the DMFC cathode. Upon solving Eq. 39-41, 44, and 51, one can find the surface coverages, cathode overpotential, water saturation, and oxygen concentration on the cathode catalyst layer. However, only the steady-state conditions are considered

$$r_{C1} - r_{C2} + r_{-C2} = 0 \quad [53]$$

$$r_{C3} - r_{C4} - r_{-C5} = 0 \quad [54]$$

$$i_{cell} - Fr_{C1} - 3r_{C2} + 3Fr_{-C2} + 4Fr_{C3} + 2Fr_{C4} = 0 \quad [55]$$

$$\frac{\alpha I}{F} + 2r_{C2} - r_{C4} - R_{H_2O} = 0 \quad [56]$$

$$R_{O_2}(\text{diffusive}) + R_{O_2}(\text{convective}) - r_{C1} - \frac{r_{C5}}{2} = 0 \quad [57]$$

Upon solving Eq. 53-57 iteratively under the given operating conditions and material variables, the steady-state values of θ_{CO}, θ_{O_2H}, η_C, s, and $C^{cc}_{O_2}$ are evaluated.

Experimental

Electrochemical characterization.— Voltage measurements were conducted using an Arbin Instruments fuel cell test station. The MEAs employed in all the experiments were assembled with 4 mg/cm^2 Pt/Ru on the anode and 4 mg/cm^2 Pt on the cathode. The active area of the MEA was 25 cm^2. Carbon cloth was used as the GDL and Nafion 117 as the membrane. The temperature maintained in all the experiments was 60°C, and the flow rate of methanol was fixed at 4 mL/min. Polarization data were recorded with cathode air supplied at 100% humidification and a constant flow rate of 500 sccm. Polarization data were obtained by setting the current density and measuring the corresponding voltage. Each current step was maintained for 5 min before it was incremented until the voltage dropped below 0.2 V.

Quantifying cathode and anode overpotentials.— The model developed here is characterized with the experimental values of the cathode and anode overpotentials. In the model, all the material parameters and operating conditions are known. However, the anode (k_{A1},k_{A2},k_{-A2}) and cathode (k_{C1},k_{C2},k_{-C2},k_{C4},k_{C5}) kinetic constants were evaluated by fitting the overpotentials from the model to that of the experiments. To accomplish this, the anode and cathode overpotentials must be measured experimentally.[36,37]

The DMFC is a two-electrode configuration where the net voltage from the fuel cell is the sum of the anode and cathode potentials. After accounting for the anode and cathode overpotentials and ohmic losses, the net voltage from the fuel cell is expressed as

$$E_{cell} = E^o - \eta_A + \eta_c - I\omega \quad [58]$$

where E^o is the open-circuit voltage of the fuel cell, which decreases with increasing temperature. Ohmic losses were evaluated from the high frequency resistance of the cell measured at each current density using a Versastat milliohmmeter at 10–50 kHz.

The anode overpotential was obtained by measuring the voltage from the fuel cell operating with methanol on the anode and hydrogen at 200 sccm on the cathode with all other operating conditions kept constant. The same MEA and fuel cell components were employed for all experiments. In this situation, the cathode served as a standard reference electrode whose potential is ~0 and the anode overpotential was evaluated as

$$\eta_A = E_{meoh/H_2} - I\omega \quad [59]$$

The cathode overpotential in the DMFC corresponds to the ORR with and without crossover effect. Overpotential from the oxygen reduction without the effect of methanol oxidation was evaluated by operating the fuel cell with H_2/O_2 as its reactants. The cell was supplied with fully humidified hydrogen at a flow rate of 500 sccm to reduce ohmic losses from membrane dehydration. The cathode overpotential without the effect of methanol oxidation is given by

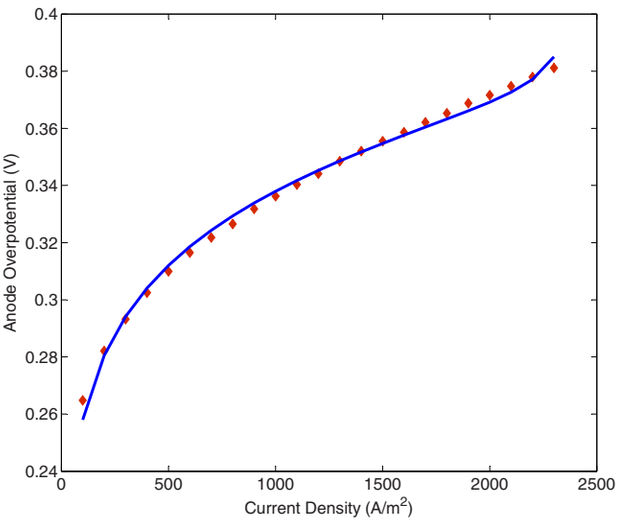

Figure 2. (Color online) Comparison of experimental and simulated anode overpotentials; the model kinetic constants were tuned to fit experimental data obtained at 2 M methanol feed concentration.

$$\eta_c(H_2/O_2) = E_{H_2/O_2} + I\omega - E^o(H_2/O_2) \quad [60]$$

The cathode overpotential was evaluated from the DMFC polarization data and from the anode overpotentials evaluated in Eq. 59 as follows

$$\eta_c = E_{meoh/O_2} + \eta_A + I\omega - E^o \quad [61]$$

Results and Discussion

Anode.— The anode overpotential obtained by solving Eq. 21-27 was fitted to the experimental anode overpotential by tuning the anode kinetic constants k_{A1}, k_{A2}, k_{-A2}, and k_{A3}. Figure 2 shows that the anode overpotential values provided by the model by fitting the kinetic constants agree well with the experimentally obtained overpotentials using 2 M methanol. The corresponding values of the fitted kinetic coefficients are $k_{A1} = 0.01317$ m/s, $k_{A2} = 8.96 \times 10^{-6}$ mol/(m^2 s), $k_{-A2} = 9.91 \times 10^4$ mol/(m^2 s), and $k_{A3} = 15.221$ mol/(m^2 s) (Table I). The anode overpotential is seen to follow the Tafel kinetics and increases with current density.

To understand the drop in voltage due to activation losses, the model was exercised at different methanol feed concentrations and the corresponding anode overpotential was obtained, as shown in Fig. 3. The kinetic constants obtained with experiments at 2 M were validated for accuracy at 1 and 4 M concentrations. The simulated overpotentials agree well with the experimental overpotentials for all current densities except for small deviations at the high end of the range. This deviation is attributed to the inaccuracy involved in

Table I. Fitted kinetic parameters for anode and cathode kinetics for cathode catalyst loading of 4 mg/cm^2 Pt/C and anode catalyst loading of 4 mg/cm^2 Pt–Ru/C.

Kinetic constants	Values
k_{A1} (m/s)	0.01317
k_{A2} [mol/(m^2 s)]	8.96×10^{-6}
k_{-A2} [mol/(m^2 s)]	9.91×10^4
k_{A3} [mol/(m^2 s)]	15.221
k_{C1} (m/s)	1.2×10^{-6}
k_{C2} [mol/(m^2 s)]	4.48×10^{-5}
k_{C4} [mol/(m^2 s)]	1.69×10^{-4}
k_{C5} [mol$^{1/2}$/(m$^{1/2}$ s)]	3233

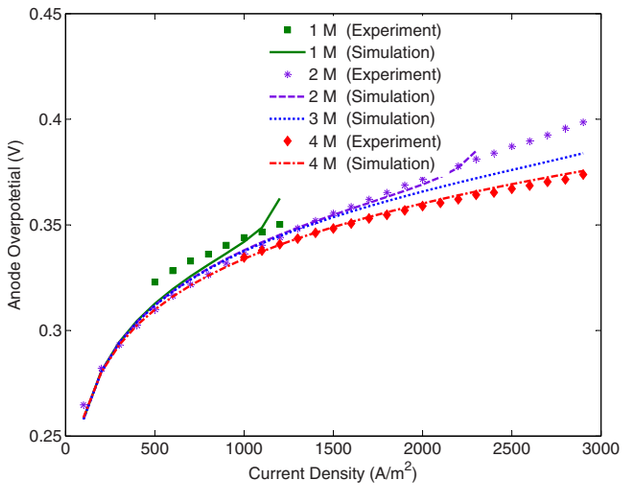

Figure 3. (Color online) Comparison of experimental and simulated anode overpotentials for various anode methanol concentrations as a function of current density.

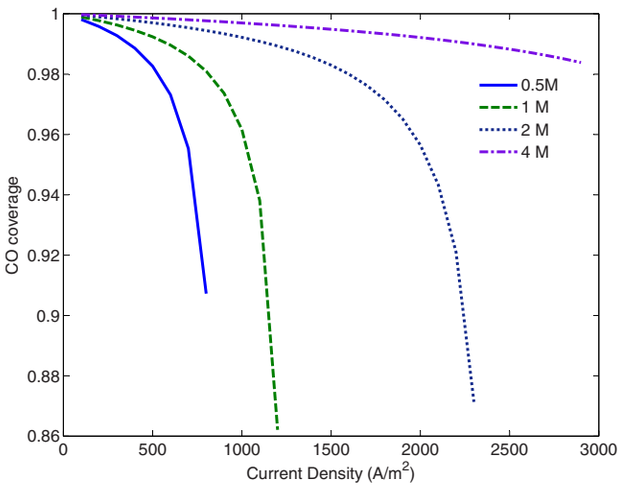

Figure 5. (Color online) Variation of CO coverage with anode methanol concentration as a function of current density.

modeling the through-plane convective molar flux of methanol in Eq. 16, which will be discussed later in this section. First, at low current densities, the anode overpotential is a weak function of the methanol feed concentration. With increasing current density, the difference between the overpotentials corresponding to different concentrations increases until ~3 M. At concentrations greater than 3 M, the overpotential becomes insensitive to concentration across the entire range of current densities. Obviously, lower overpotentials are associated with better cell performance. While Fig. 3 indicates that higher concentrations would improve the cell performance, this improvement is countered by the methanol crossover effect, which also increases as the methanol feed concentration is increased.

With the complete DMFC anode model, additional simulations were performed to study the influence of various parameters and operating conditions. The variation of the catalyst coverage of θ_{CO} and θ_{OH} with current density is plotted in Fig. 4 at a methanol concentration of 2 M. The CO coverage (θ_{CO}) decreases with current density, while the OH coverage (θ_{OH}) increases with current density. However, while the CO coverage values range between 1 and 0.7, the OH coverage is negligible. This can be understood from the reaction steps and the magnitude of the corresponding kinetic

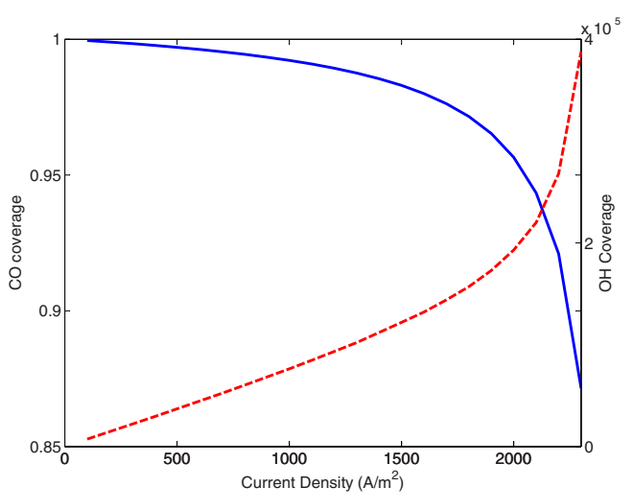

Figure 4. (Color online) Variation of CO and OH coverages with current density at 2 M concentration.

constants. It is well known that methanol has a high affinity toward Pt, and most of the Pt sites are occupied, forming PtCO. With increasing current density, there is a demand for the oxidation of methanol, and hence, more PtCO oxidizes by the desorption of CO from platinum.

As discussed in the Anode kinetic model section, in parallel to methanol adsorption on Pt, water also adsorbs on Ru. This reaction step is reversible, and the value of the forward kinetic constant (k_{A2}) is smaller than the backward kinetic constant (k_{-A2}). RuOH also participates with PtCO in the third reaction, and its kinetic constant (k_{A3}) is higher than the second reaction's kinetic constant. Hence, we can infer that water is adsorbed on demand and directly reacts with CO_{ads}. Figure 4 shows that the magnitude of the OH coverage is smaller than that of PtCO. Low water coverage on the Ru catalyst layer would indicate that the ratio of Ru to Pt can be reduced while still maintaining the electrical efficiency of the fuel cell.

The methanol adsorbate on Pt catalyst (θ_{CO}) is considered as a form of storage of methanol.[38] During an intermittent supply of methanol, CO on Pt will act as a feed for the current. The presence of θ_{CO} represents an incomplete oxidation of methanol, poisoning the catalyst. Figure 5 shows θ_{CO} with increasing current density at various concentrations. At lower concentrations, the CO coverage drops rapidly with current density. The first step is methanol chemisorption; therefore, it is rate-limiting at high concentrations. However, at higher concentrations, the drop in CO coverage is less pronounced. At concentrations higher than 2 M, most of the Pt sites are saturated with CO and any available methanol will increase the propensity for methanol crossover. Because we are using a bimetallic Pt–Ru catalyst on the anode, the Ru sites serve for water adsorption and desorption. If only Pt was used as a catalyst, Pt poisoning would push the methanol reaction to reaction-limiting conditions.

At steady state, along with CO adsorbed on the Pt catalyst, methanol also resides in the anode catalyst layer. The presence of methanol in the anode catalyst layer leads to methanol crossover from the anode to the cathode. Figure 6 shows the concentration of methanol in the anode catalyst layer with increasing feed concentration at different current densities. With increasing current density, more methanol reacts on the anode catalyst, causing a drop in the local average concentration. However, methanol is still available at the anode catalyst layer through diffusion and convection across the anode GDL. As described in the Two-phase modeling in the anode GDL section, the diffusive and convective components of methanol molar flux toward the catalyst layer are evaluated and plotted in Fig. 7.

The convective molar flux of methanol increases with current

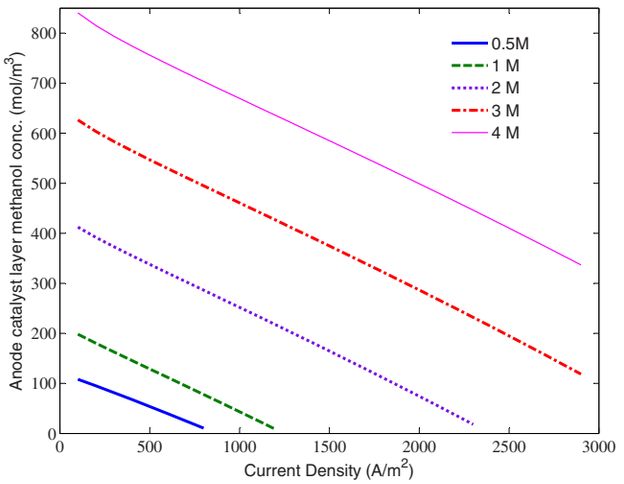

Figure 6. (Color online) Variation of methanol concentration in the anode catalyst layer with anode feed methanol concentration as a function of current density.

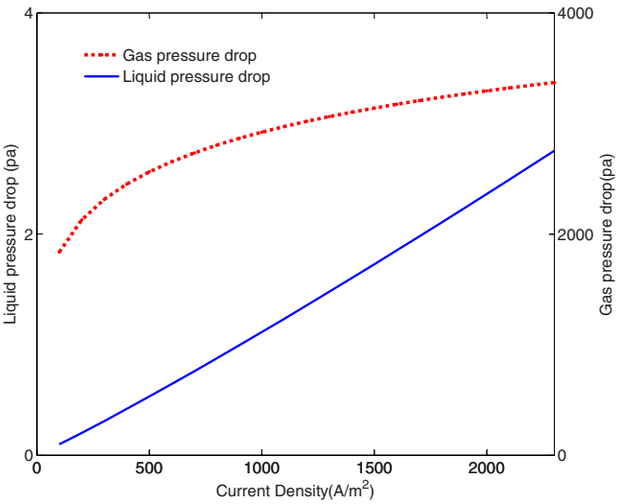

Figure 8. (Color online) Variation of liquid and gas pressure drops through the anode GDL with current density at 2 M feed concentration.

density up to a maximum value and then drops. This nonmonotonic behavior is due to the opposing trends of methanol concentration and liquid pressure drop in Eq. 16. With increasing current density, more CO_2 is produced, which moves to the anode flow field. The volume occupied by the CO_2 gas is replaced with liquid repetitively, which increases the liquid convection toward the catalyst layer. The flow of gas away from the catalyst layer is correlated with the liquid flow toward the catalyst layer. The flow of the two phases sets up corresponding pressure drops across the GDL, as shown in Fig. 8. The gaseous pressure drop is a result of capillary forces in the GDL pores. The variation of capillary pressure drop with current density is shown in Fig. 9. The convective mass transport of methanol toward the anode catalyst layer described in Eq. 16 is approximate and tends to underestimate the actual value. Ideally, the mixing effect due to the generation of bubbles and the inertial effect due to bubble movement have to be considered for describing through-plane convection. Therefore, simulations adopting Eq. 16 would tend to underestimate the through-plane molar flux of methanol toward the anode catalyst layer and result in higher anode overpotentials. This effect is more noticeable at high current densities due to higher CO_2 generation. Therefore, in Fig. 3 the simulated overpotentials do not agree with the experimental overpotentials at high current densities.

In contrast to the trend of liquid convection, the concentration of methanol on the anode catalyst layer drops with current density (Fig. 6). This nonmonotonic behavior of convective molar flux is due to the opposing trends of methanol concentration and liquid pressure drop in Eq. 16. Our simulations indicate that the diffusive component of molar flux toward the catalyst layer is larger than the convective molar flux. Additionally, the diffusive molar flux increases slightly with current density in Fig. 7. In contrast, it is often reported that the diffusive flux of methanol should decrease with current density[7,39] as the higher production of CO_2 gas would block the GDL pores, reducing the area available for diffusion. We indeed observe in Fig. 10 that the fraction of CO_2 blocking the GDL pores increases with current density. However, along with increasing gas fraction in the pore volume, the concentration gradient of methanol across the GDL also increases (Eq. 15) with current density. The effects of increasing pore gas fraction and concentration gradient oppose each other, with the concentration gradient effect being more dominant. As a result, the diffusive flux of methanol increases

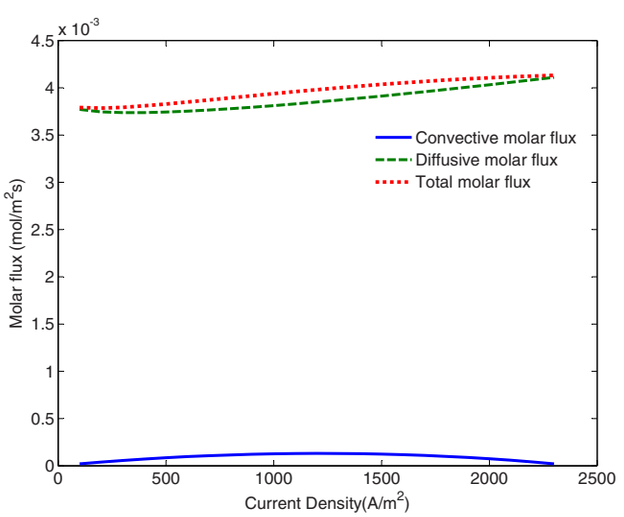

Figure 7. (Color online) Comparison of convective, diffusive, and total molar fluxes of methanol through the anode GDL at 2 M feed concentration as a function of current density.

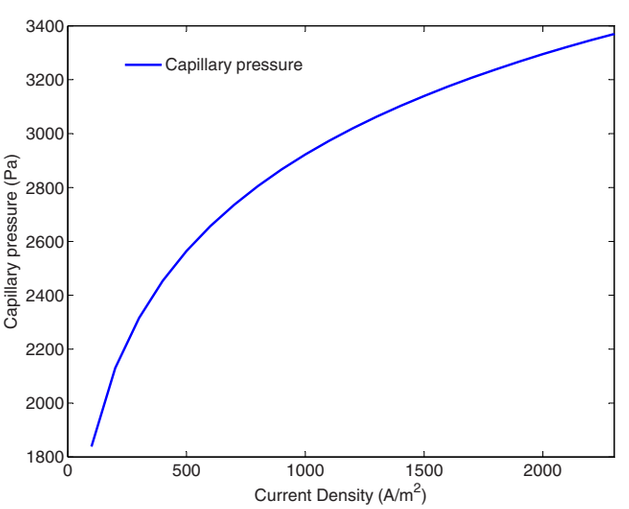

Figure 9. (Color online) Variation of capillary pressure drop through the anode GDL with current density at 2 M feed concentration.

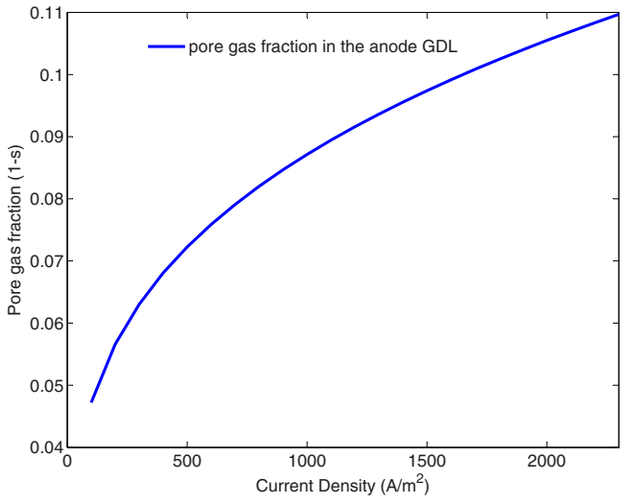

Figure 10. (Color online) Variation of anode GDL pore gas fraction with current density at 2 M feed concentration.

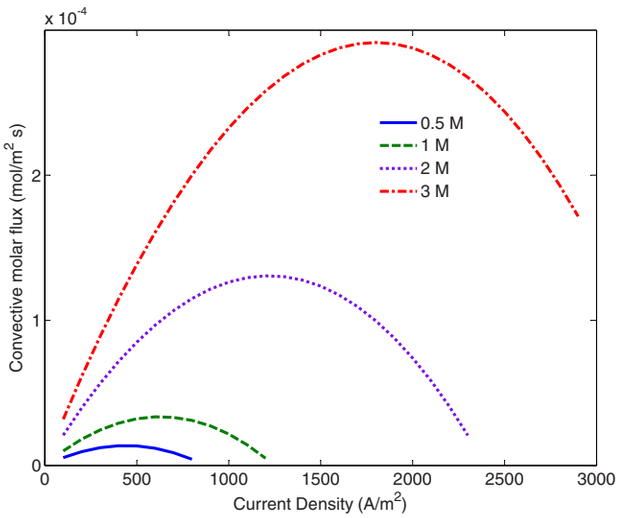

Figure 12. (Color online) Variation of methanol convective flux with concentration as a function of current density.

slightly with current density. Furthermore, the deterioration in diffusive flux by bubble blocking is also smaller than the increase in liquid convection arising from gas motion. Hence, it is concluded that the generation of bubbles improves fuel cell performance.

The important discovery in our observation is that the produced bubbles actually enhance the performance of the fuel cell. Our observations and conclusions are only applicable to the experimental conditions and material parameters used in our experiments. Detailed analysis of bubble flow in the anode channel and its influence on performance was explored by Kulikovsky et al.[13]

We have also simulated and plotted the diffusive mass flux of methanol toward the catalyst layer at different concentrations as a function of current density. Figure 11 indicates that at a given current density, the diffusive flux increases with the feed concentration of methanol. This result is easy to understand because a higher feed concentration sets up a steeper gradient which drives the diffusive flux. It is also observed at 1 M that the diffusive flux is seen to increase linearly with current density. However, with concentrations greater than 2 M, the diffusive flux is seen to drop moderately at low current densities, which is followed by a steady increase. At higher concentrations, the effects of GDL pore blockage by increasing gas fraction dominates the concentration gradient with current density and hence at diffusive flux drops with current density.

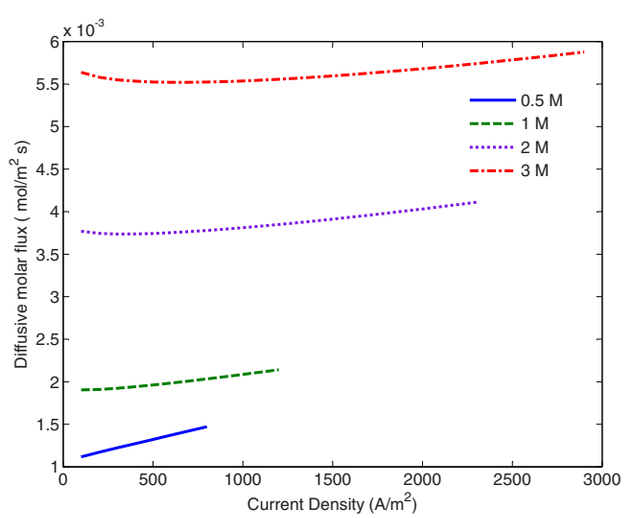

Figure 11. (Color online) Variation of methanol diffusive flux with concentration as a function of current density.

Similarly, Fig. 12 shows the convective flux of methanol toward the catalyst layer at different feed concentrations. The maximum value of convective molar flux is seen to increase with methanol feed concentration. This maximum value also shifts toward larger current densities for higher methanol concentrations. Our DMFC experiments employed an active system to replenish the methanol solution in the flow field, thereby maintaining a constant feed concentration throughout the experiment. In such active systems, both the diffusive and convective fluxes remain constant in time. However, a passive methanol delivery system can result in a methanol feed concentration that drops with time, implying that both the diffusive and the convective fluxes decrease with time, and therefore, different dynamics are observed.

Cathode.— Cathode kinetic parameters were estimated by fitting the solution of Eq. 53-57 to the experimentally measured value of the cathode overpotential. The methodology adopted is described in the Quantifying cathode and anode overpotentials section. Kinetic constants k_{C1} and k_{C2} are evaluated by matching the simulated cathode overpotential without crossover to the experimentally measured cathode overpotential from the H_2/O_2 cell. The values of the constants determined were $k_{C1} = 1.2 \times 10^{-6}$ m/s and $k_{C2} = 4.48 \times 10^{-5}$ mol/(m^2 s) (Table I). These values for k_{C1} and k_{C2} were inserted into the complete cathode model whose output was now matched to the experimentally measured cathode overpotential from the DMFC. After performing a sensitivity analysis to minimize error, the remaining cathode kinetic constants were obtained as $k_{C4} = 1.69 \times 10^{-5}$ mol/(m^2 s) and $k_{C5} = 3233$ [mol/(m s^2)]$^{0.5}$. The values of the kinetic constants allow us to interpret the nature of each corresponding reaction. For example, from the values of k_{C4} and k_{C5}, methanol undergoes chemical reaction at a faster rate than the electrochemical reaction rate. Additional details about the kinetic constants and the nature of the reactions can be found in a separate publication from our group.[33]

Figure 13 shows the plot of the experimental and simulated cathode overpotentials for the 2 M concentration case. Because the cathode overpotential is always negative, a larger magnitude corresponds to a further drop in the overall cell voltage. The detrimental effect of the crossover is confirmed by the observation that the DMFC cathode overpotential is significantly larger in magnitude than the H_2/O_2 value. The magnitude of the cathode overpotential

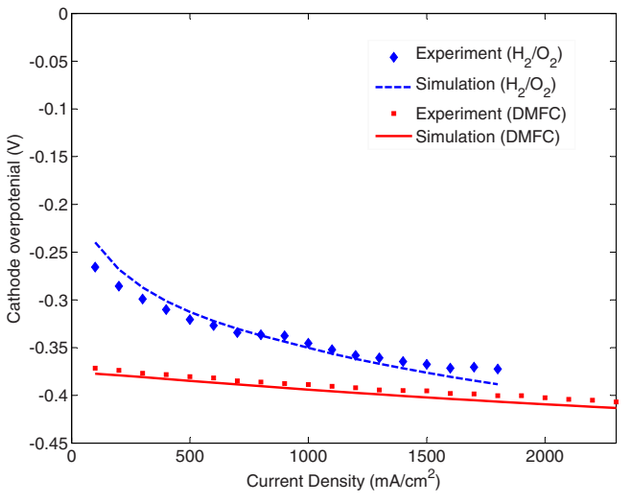

Figure 13. (Color online) Comparison of experimental and simulated values of cathode overpotentials as a function of current density at 2 M feed concentration.

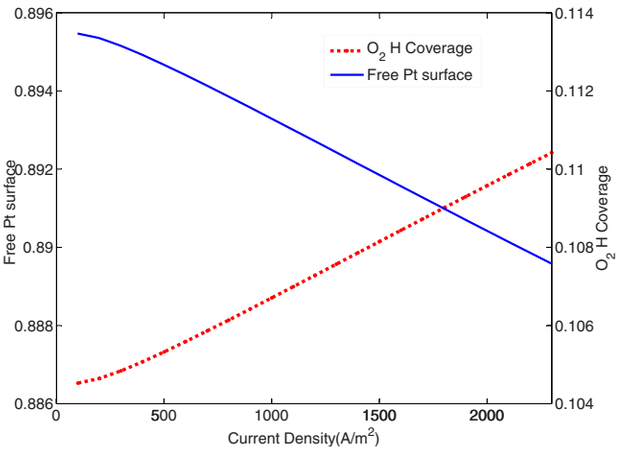

Figure 15. (Color online) Variation of adsorbed intermediates with current density at an air flow rate of 500 sccm in the cathode flow field.

increases with current density for both cases due to the ORR. The difference between the two curves diminishes as high current density is increased. At higher current densities, methanol is consumed at a proportionally higher rate in the anode catalyst layer and so less methanol is available for crossover to the cathode catalyst layer. Hence, the effect of methanol oxidation on the cathode overpotential is reduced at high current densities.

Increasing the feed methanol concentration in the anode compartment also increases the overpotential losses. Figure 14 indicates that increasing the methanol concentration from 1 to 4 M increases the overpotential by 90 mV at 50 mA/cm^2. In contrast, Fig. 3 shows that the anode overpotential decreases with the feed concentration. Due to the opposing effect of methanol concentration on the anode and cathode overpotentials, it is evident that an optimal value of concentration should exist for each current density for which the overall cell voltage is maximized.[5]

The rate of each reaction in the cathode reaction set can be evaluated from the kinetic constants, the overpotential, concentration, and intermediate coverages. Figure 15 shows the free platinum surface and O_2H coverage on the catalyst as a function of current density. From the reaction set, the intermediate adsorbants are PtCO and PtO_2H. However, our simulations indicate that 89% of the Pt surface is not covered with any intermediates. High cathode catalyst loading (4 mg/cm^2) and the presence of air would lead to increasing desorption rates. In addition, only 11% of the catalyst sites are occupied with PtO_2H intermediates. Our assumption of complete oxidation of methanol on the cathode catalyst layer also leads to a negligible amount of CO coverage. The O_2H coverage increases with current density, whereas the amount of free Pt surface is virtually constant.

The chemical reaction of methanol and oxygen reduction proceed with the transport of oxygen to the cathode catalyst layer. The different modes of oxygen transport toward the catalyst layer were described in the Two-phase modeling in the cathode GDL of DMFC section. The diffusive, convective, and total molar flux of oxygen toward the catalyst layer were evaluated using Eq. 45 and 51 and are plotted in Fig. 16. Our simulations have revealed that the diffusive mass flux in DMFCs is $\sim 10^3$ times greater than the convective mass flux. In contrast, under similar operating conditions, convective transport exceeds diffusion in the case of the H_2/O_2 fuel cell. The convective transport occurs in-plane in the GDL underneath the land, whereas diffusion occurs through-plane in the GDL under the channel of the flow field. From Fig. 16, the diffusive molar flux

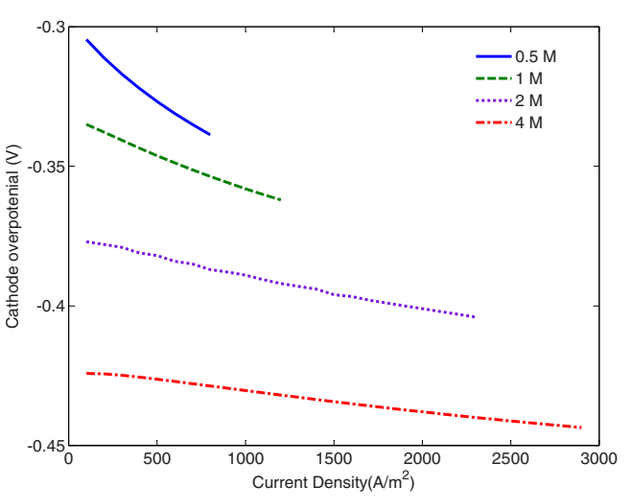

Figure 14. (Color online) Simulated cathode overpotentials as a function of current density at various feed concentrations.

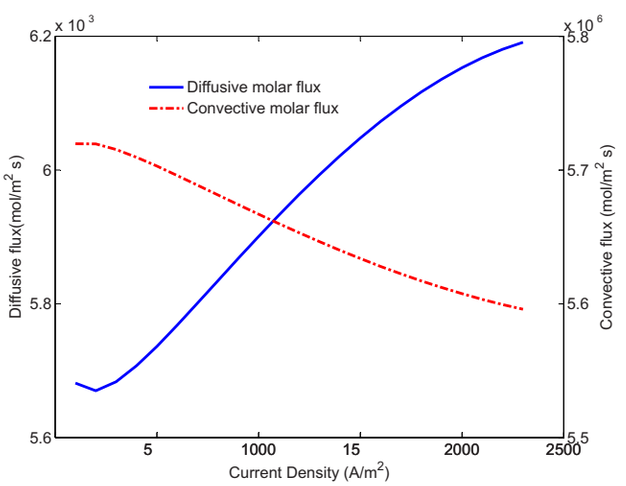

Figure 16. (Color online) Variation of convective and diffusive molar flux of oxygen in the cathode with current density at an air flow rate of 500 sccm in the cathode flow field.

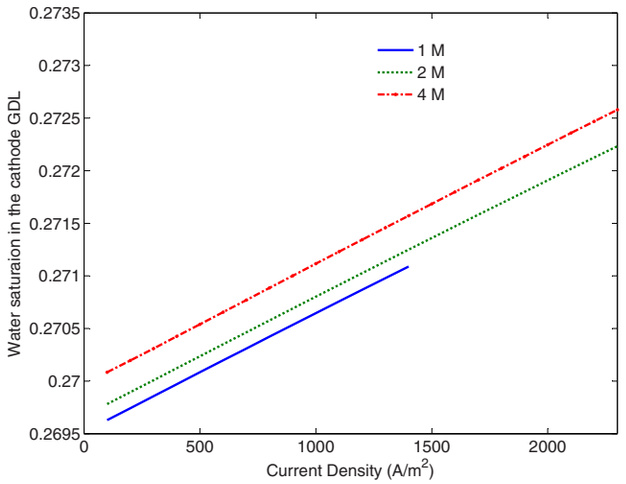

Figure 17. (Color online) Variation of water saturation in the cathode GDL with current density at an air flow rate of 500 sccm.

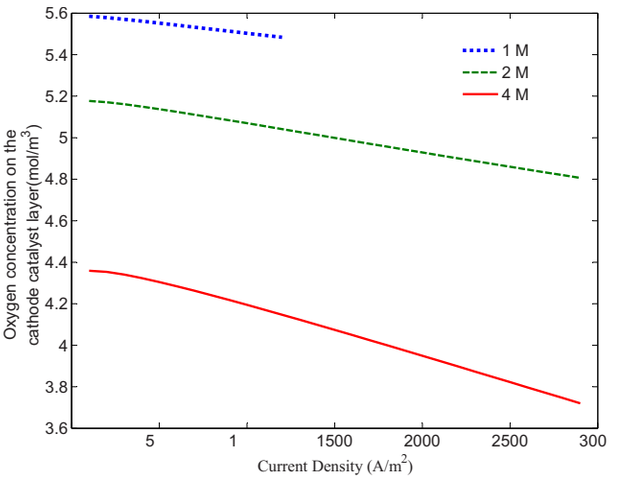

Figure 18. (Color online) Comparison of oxygen concentration on the cathode catalyst layer at various anode methanol concentrations as a function of current density.

increases with current density, whereas the convective molar flux decreases. With increasing current density, the oxygen concentration on the cathode catalyst layer drops, which reduces the convective mass transport toward the catalyst layer. However, lowering the concentration on the catalyst layer increases the concentration gradient across the GDL, and hence, the molar diffusive flux is seen to increase steadily.

The diffusive molar flux of oxygen is a function of the concentration gradient through the cathode GDL as well as the water saturation within the GDL. Water originating in the catalyst layer is expelled to the cathode flow field by capillary forces; however, at steady state, some water blocks the GDL pores. Figure 17 shows the water saturation in the GDL at different anode concentrations as a function of current density. More water is produced at higher current densities, and hence, the pore water fraction is seen to increase linearly. Crossover methanol oxidation on the cathode catalyst also produces water, and hence, due to high crossover, the water saturation in the GDL increases at higher feed concentrations. Its contribution to total saturation is small; however, with increasing water saturation in the GDL, the diffusion rates across the GDL decrease. Figure 16 shows the opposite result, implying that a strong counterbalancing concentration gradient would have to be established with increasing current density. This conjecture is verified by plotting the oxygen concentration on the cathode catalyst layer in Fig. 18. The oxygen concentration on the cathode catalyst indeed decreases with current density, implying that the concentration gradient is greater. Assuming the oxygen in the flow field is in 100% humidified air, its bulk concentration is evaluated to be 6 mol/m^3. Figure 18 also shows that the oxygen concentration on the cathode catalyst decreases significantly with anode methanol concentration due to the consumption of oxygen by methanol oxidation.

Figure 19 shows the ratio of oxygen consumed in reaction r_{C5} (chemical oxidation of methanol) to the oxygen consumed in reaction r_{C1} (electroreduction of oxygen). A large fraction of oxygen reacts with methanol through chemical pathway. For example, at low current densities and high methanol concentration, $\sim$30% of the total oxygen transported to the catalyst layer is consumed by methanol oxidation. Therefore, oxygen electroreduction suffers from considerable oxygen mass transport limitations. The degradation in cathode performance at high methanol concentration is due to mixed oxidation potential. However, our simulations reveal that apart from depolarizing the cathode, the limitations of oxygen mass transport also degrade the cathode performance. In a regular H_2/O_2 cathode, mass transport limitations are readily identified by decreasing the air flow rate and observing a corresponding drop in performance. However, because diffusion is so dominant in DMFCs compared to convection, it is difficult to experimentally identify the mass transport limitations. Hence, our simulations provide critical new insights into the cathode mass transport process.

Conclusions

A mathematical model incorporating the kinetic and mass transfer process in DMFCs has been developed. One of the main goals is to predict the steady-state values of overpotentials and other parameters with varying operating conditions. Models were developed for the two-phase flow in the anode and cathode GDLs and coupled with the reaction kinetics. The anode and cathode kinetic coefficients were obtained by fitting the simulated overpotentials with the experimentally measured values. After the model was validated, simulations were performed to quantify various parameters during the steady-state operation of the DMFC. Subsequently, the evaluated parameters were analyzed as a function of the operating conditions to gain insight into the underlying physicochemical processes.

The anode overpotential was independent of the kinetic and mass transfer processes in the cathode compartment. However, the cathode overpotential is coupled with the crossover of methanol from

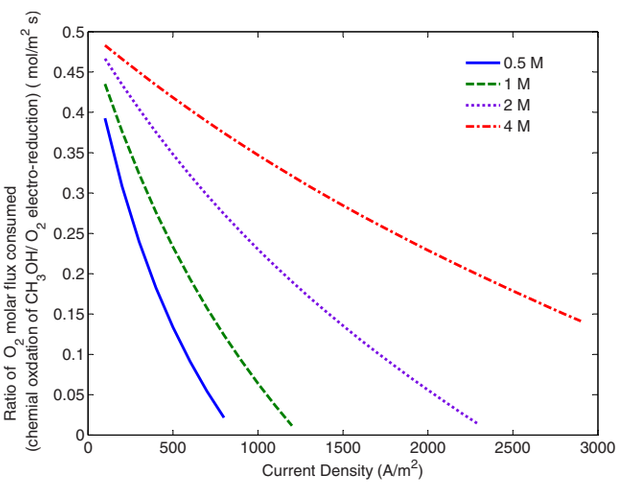

Figure 19. (Color online) Comparison of the ratio of oxygen consumed in the methanol chemical reaction to oxygen electroreduction at various anode methanol concentrations as a function of current density.

the anode compartment. The anode overpotential is a strong function of methanol feed concentration at higher current densities. The platinum surface is poisoned with the intermediate PtCO, whereas fewer Ru sites were occupied by RuOH. Our simulations show that raising the concentration above 2 M causes most of the Pt sites to become saturated with CO and does not help in improving the anode overpotential. To quantify the availability of methanol on the anode catalyst layer, different modes of transport of methanol across the anode GDL were formulated and evaluated. Convective flux increases with current density, while the diffusive flux does not change significantly. However, diffusion constituted the major transport mechanism. This result has led to the discovery that the improvement in performance seen by bubble convection dominates over the reduction in diffusion due to bubbles blocking the GDL. Hence, we conclude that for the operating conditions and materials employed in our experiments, CO_2 bubble generation enhances performance.

The experimentally evaluated cathode overpotential, with and without the effect of mixed methanol oxidation, shows that significant deterioration in voltage is caused by the presence of crossover methanol on the cathode catalyst layer. Therefore, the magnitude of the cathode overpotential increases with anode methanol concentration. Our model for cathode reaction kinetics incorporates both the chemical and electrochemical oxidation of methanol on the cathode catalyst. Due to consumption of oxygen by the chemical oxidation of methanol on the cathode catalyst layer, the oxygen concentration drops significantly with anode methanol concentration. The low concentration of oxygen on the cathode catalyst layer implies a reduced mean oxygen concentration in the cathode GDL, which reduces the in-plane convective mass flux in the GDL. Because the reaction kinetics of oxygen electroreduction and methanol oxidation on the Pt catalyst are strong, lower values of intermediate coverages are observed.

Our model has been shown to produce results that agree with experimental values. It is also able to provide key insights into processes that are difficult to quantify experimentally. Hence, our model is useful in improving our overall understanding of the kinetic and mass transfer processes in DMFCs.

Acknowledgments

This research was supported by the Delaware Department of Natural Resources and Environmental Control, the Federal Transit Administration, and the Max Planck Society.

University of Delaware assisted in meeting the publication costs of this article.

List of Symbols

a	charge transfer coefficient, 0.5
A	active area of the fuel cell, 25×10^{-4} m^2
b	channel width of the serpentine flow field, 0.8×10^{-3} m
c_A	anode catalyst layer dielectric capacitance, F m^{-2}
c_C	cathode catalyst layer dielectric capacitance, F m^{-2}
c_{pt}^{ac}	surface concentration of platinum sites on anode catalyst layer, mol m^{-2}
c_{ru}^{ac}	surface concentration of ruthenium sites on anode catalyst layer, mol m^{-2}
c_{pt}^{cc}	surface concentration of platinum sites on cathode catalyst layer, mol m^{-2}
C_{CO_2}	concentration of carbon dioxide in the anode catalyst layer, mol m^{-3}
C_o	concentration of methanol in the supplied solution, mol m^{-3}
C_{meoh}^{ac}	concentration of methanol in the anode catalyst layer, mol m^{-3}
$C_{O_2}^{cc}$	concentration of oxygen on the cathode catalyst layer, mol m^{-3}
d_{aGDL}	thickness of anode GDL, 3×10^{-4} m
d_{cGDL}	thickness of cathode GDL, 3.6×10^{-4} m
d_{mem}	thickness of the membrane, 1.78×10^{-4} m
$D_{meoh,water}$	diffusion coefficient of methanol in water, 3×10^{-9} m^2 s^{-1}
D_{meoh}^{GDL}	diffusion coefficient of methanol in the GDL, m^2 s^{-1}
D_{meoh}^{mem}	diffusion coefficient of methanol in the membrane, 1.56×10^{-9} m^2 s^{-1}
F	Faraday's constant, 96,485 A s mol^{-1}
g_{CO}	inhomogeneity/interaction factor for Frumkin/Temkin adsorption on Pt, 11
g_{OH}	inhomogeneity/interaction factor for Frumkin/Temkin adsorption on Ru, 0.43
h	depth of the serpentine channel, 10^{-3} m
i_{cell}	current density withdrawn from the cell, A m^{-2}
$J(s)$	Leverette function
k_i	kinetic constant of a reaction step i on the catalyst layer
k_{rg}	relative permeability of the gas phase
k_{rl}	relative permeability of the liquid phase
K	absolute permeability of the GDL, 10^{-13} m^2
K_c	permeability of the flow field channel, 3×10^{-8} m^2
K_i	in-plane permeability of the GDL, 5×10^{-13} m^2
L	length of the serpentine channel, 5×10^{-2} m
m_{H_2O}	mass of water accumulation in the anode catalyst layer, kg
M_{H_2O}	Mw of water, 18×10^{-3} kg
M_{meoh}	Mw of methanol, 32×10^{-3} kg
N_c	number of channels in the serpentine flow field, 31
P	pressure in the GDL, Pa
P_c	capillary pressure in the GDL, Pa
Q	flow rate of air supplied to the cathode inlet, m^3
r	reaction rate with respect to total catalyst pore surface, mol m^{-2} s^{-1}
R	ideal gas constant, 8.314 J mol^{-1} K^{-1}
s	liquid saturation in the GDL
T	temperature of the fuel cell, K
u	superficial areal velocity vector, m s^{-1}
$u(x)$	mean velocity of oxidant along the length (x direction) in the channel, m s^{-1}
$v(x)$	mean velocity of oxidant along the length (x direction) in the GDL under the land, m s^{-1}
V_{GDL}	mean velocity of oxidant in the GDL under the land
V^{ac}	volume of the anode catalyst layer, m^3
V^{cc}	volume of the cathode catalyst layer, m^3
w	land width of the serpentine flow field, 0.8×10^{-3} m

Greek

α	electro-osmotic drag coefficient of water in Nafion 117 membrane, 2.5
β_{CO}	symmetry parameter for Frumkin/Temkin adsorption on Pt
β_{OH}	symmetry parameter for Frumkin/Temkin adsorption on Ru
ϵ	porosity of the GDL
η	overpotential, V
μ_g	viscosity of the carbon dioxide gas, 1.68×10^{-5} Pa s
μ_l	viscosity of the methanol solution, 0.547×10^{-3} Pa s
θ_c	contact angle of the GDL
θ_{CO}	CO surface coverage on Pt catalyst layer
θ_{CO}^{cc}	coverage of CO on cathode platinum catalyst layer
θ_{OH}	OH surface coverage on Ru catalyst layer
$\theta_{O_2H}^{cc}$	coverage of O_2H on cathode platinum catalyst layer
ρ_g	density of carbon dioxide gas, 1.98 kg m^{-3}
ρ_l	density of the liquid, 1000 kg m^{-3}
ω	ohmic resistance of the fuel cell, ohms

Subscript

A	on the anode compartment
A1	reaction step 1 on the anode catalyst layer
A2	forward reaction step 2 on the anode catalyst layer
−A2	backward reaction step 2 on the anode catalyst layer
A3	reaction step 3 on the anode catalyst layer
C1	reaction step 1 on the cathode catalyst layer
C2	forward reaction step 2 on the cathode catalyst layer
−C2	backward reaction step 2 on the cathode catalyst layer
C3	reaction step 3 on the cathode catalyst layer
C4	reaction step 4 on the cathode catalyst layer
C5	reaction step 5 on the cathode catalyst layer
g	gas
l	liquid

Superscript

ac	on the anode catalyst layer
cc	on the cathode catalyst layer

References

1. E. C. Weigert, S. Arisetty, S. G. Advani, A. K. Prasad, and J. G. Chen. *J New Mater. Electrochem. Syst.*, **11**, 243 (2008).
2. K. Ren, T. A. Zawodzinski, and S. Gottesfeld, *J. Electrochem. Soc.*, **147**, 466 (2000).
3. H. Dohle, J. Divisek, J. Mergel, H. F. Oetjen, C. Zingler, and D. Stolten, *J. Power Sources*, **105**, 274 (2002).

4. G. Jewett, Z. Guo, and A. Faghri, *J. Power Sources*, **168**, 434 (2007).
5. S. Arisetty, C. A. Jacob, A. K. Prasad, and S. G. Advani, *J. Power Sources*, **187**, 415 (2009).
6. T. Vidakovic, M. Christov, and K. Sundmacher, *J. Electroanal. Chem.*, **580**, 105 (2005).
7. H. Yang, T. S. Zhao, and Q. Ye, *J. Power Sources*, **139**, 79 (2005).
8. V. Gogel, Z. Yongsheng, K. A. Friedrich, L. Jorissen, and J. Garche, *J. Power Sources*, **127**, 172 (2004).
9. K. Scott, C. Jackson, and P. Argyropoulos, *J. Power Sources*, **161**, 885 (2006).
10. K. Scott, W. M. Taama, P. Argyropoulos, and K. Sundmacher, *J. Power Sources*, **83**, 204 (1999).
11. K. Scott, W. M. Taama, S. Kramer, P. Argyropoulos, and K. Sundmacher, *Electrochim. Acta*, **45**, 945 (1999).
12. A. A. Kulikovsky, *Electrochem. Commun.*, **5**, 530 (2003).
13. A. A. Kulikovsky, *Electrochem. Commun.*, **7**, 237 (2005).
14. W. W. Yang and T. S. Zhao, *Electrochim. Acta*, **52**, 6125 (2007).
15. Z. H. Wang and C. Y. Wang, *J. Electrochem. Soc.*, **150**, A508 (2003).
16. U. Krewer, H. K. Yoon, and H. T. Kim, *J. Power Sources*, **175**, 760 (2008).
17. K.-M. Yin, *J. Power Sources*, **179**, 700 (2008).
18. P. S. Kauranen, E. Skou, and J. Munk, *J. Electroanal. Chem.*, **404**, 1 (1996).
19. A. B. Anderson and N. M. Neshev, *J. Electrochem. Soc.*, **149**, E383 (2002).
20. D. Kardash, C. Korzeniewski, and N. Markovic, *J. Electroanal. Chem.*, **500**, 518 (2001).
21. O. Antoine, Y. Bultel, and R. Durand, *J. Electroanal. Chem.*, **499**, 85 (2001).
22. G. Jerkiewicz, G. Vatankhah, J. Lessard, M. P. Soriaga, and Y. S. Park, *Electrochim. Acta*, **49**, 1451 (2004).
23. J. Rossmeisl, G. S. Karlberg, T. Jaramillo, and J. K. Norskov, *Faraday Discuss.*, **140**, 337 (2008).
24. U. Krewer, M. Christov, T. Vidakovic, and K. Sundmacher, *J. Electroanal. Chem.*, **589**, 148 (2006).
25. U. Pasaogullari and C. Y. Wang, *J. Electroanal. Chem.*, **151**, A399 (2004).
26. M. M. Mezedur, M. Kaviany, and W. Moore, *AIChE J.*, **48**, 15 (2002).
27. M. M. Tomadakis and S. V. Sotirchos, *AIChE J.*, **39**, 397 (1993).
28. S. Li, L. J. Lee, and J. Castro, *J. Compos. Mater.*, **36**, 1709 (2002).
29. J. H. Nam and M. Kaviany, *Int. J. Heat Mass Transfer*, **46**, 4595 (2003).
30. C. Xu and T. S. Zhao, *J. Power Sources*, **168**, 143 (2007).
31. W. Vielstich, V. A. Paganin, F. H. B. Lima, and E. A. Ticianelli, *J. Electrochem. Soc.*, **148**, A502 (2001).
32. V. A. Paganin, E. Sitta, T. Iwasita, and W. Vielstich, *J. Appl. Electrochem.*, **35**, 1239 (2005).
33. S. Arisetty, U. Krewer, A. K. Prasad, and S. G. Advani, Electrochim. Acta, Accepted.
34. P. S. Kauranen and E. Skou, *J. Electroanal. Chem.*, **408**, 189 (1996).
35. J. P. Feser, A. K. Prasad, and S. G. Advani, *J. Power Sources*, **161**, 404 (2006).
36. S. C. Thomas, X. Ren, S. Gottesfeld, and P. Zelenay, *Electrochim. Acta*, **47**, 3741 (2002).
37. G. Li and P. G. Pickup, *Electrochim. Acta*, **49**, 4119 (2004).
38. T. Schultz, U. Krewer, and K. Sundmacher, *J. Power Sources*, **165**, 138 (2007).
39. S. Arisetty, S. G. Advani, and A. K. Prasad, *Heat Mass Transfer*, **44**, 1199 (2008).